Pilotstudie zur $K_S^0 \to \pi^+\pi^-$-Identifikation in der Reaktion $\gamma n \to K^0\Sigma^0$ mit dem BGOOD-Experiment

Eva Tillmann

Bachelorarbeit in Physik

angefertigt im Physikalischen Institut

vorgelegt der

Mathematisch-Naturwissenschaftlichen Fakultät

der

Rheinischen Friedrich-Wilhelms-Universität

Bonn

Juni 2024

Ich versichere, dass ich diese Arbeit selbstständig verfasst und keine anderen als die angegebenen Quellen und Hilfsmittel benutzt, sowie die Zitate kenntlich gemacht habe.

Bonn, ...
Datum

....,
Unterschrift

1. Gutachter*in: Prof. Hartmut Schmieden
2. Gutachter*in: Dr. Thomas Jude

Contents

1 Introduction

To this day, the ground states and lower excitations of hadrons can successfully be described by assuming them to be quark and antiquark, or three-quark-constructs (e.g. mesons and baryons). However at higher excitations, this model does not fit the observations. One explanation could be multiquark structures, for example consisting of two quarks and antiquarks $q\bar{q}q\bar{q}$ or four quarks and one antiquark $qqqq\bar{q}$. The existence of these multiquark structures have been concluded from multiple experiments such as Belle [1] and LHCb [2]. The inner structure however still remains unclear.

A current prediction that would fundamentally back the existence of multiquark structures in the strange quark sector refers to a peak at $1750\,\mathrm{MeV}$ beam energy in the reaction $\gamma n \rightarrow \Sigma^0 K^0$ and was investigated in the doctoral thesis of K. Kohl at the BGOOD-experiment [3]. While the available statistical precision did not allow to confirm or reject the predicted peak, the shape and position of the peak were consistent with the initial prediction and lay the foundation of the presented study.

Explicitly, this thesis studies the possibility of extending the analysis to the charged decay of the K^0 ($K^0 \rightarrow \pi^+\pi^-$).

As the background of this study could strongly hint at the existence of said multiquark structures in the strange quark sector, this work begins with a more extended motivation. This is followed by an overview of the experimental setup and the analysis tools, before the extended decay path of the final state particles and the particle selection are explained. The main part of this work - the reconstruction of the decay particles with the corresponding selection cuts and conditions - will be discussed thereafter.

Finally, there will be an outlook how this thesis could be extended.

2 Motivation

The conventional quark model can be used to describe two- and three-quark constructs (mesons ($q\bar{q}$) and baryons (qqq)), called hadrons. Quarks are bound by the strong color force, described by Quantum Chromo Dynamics.

While the conventional quark model can predict the ground states of mesons and baryons, it fails to explain higher lying states and predicts additional states at high masses than have been observed ($\rightarrow$ missing resonances). Even at the lowest excitations some discrepancies are observed. For example, according to the conventional quark model, the lowest excited nucleon should have a spin parity of $1/2^-$. However, the lowest experimentally observed excited state has a spin parity of $1/2^+$ (N(1440)) [4].

There are currently two approaches that mainly vary in regard to the degrees of freedom. The first theory postulates the existence of compact multiquarks, meaning a compact bound object of more than three quarks (e.g. $qqqq\bar{q}$).

The second theory focuses on the possibility of multiquark structures on a hadronic level, considering these compositions to be molecular bindings ($\rightarrow$ hadronic molecules), comparable to nucleons binding together (e.g. $(qqq)(q\bar{q})$) (for a review see [5]).

The existence of multiquark objects in the charm and bottom quark sector has been validated in multiple experiments. In 2003, the Belle Collaboration first identified the $X(3872)$ as a tetra-quark structure ($q\bar{q}q\bar{q}$) [1], and in 2019 $P_C(4312)$ and $P_C(4450)$ were shown to be penta-quark objects ($qqqq\bar{q}$) by LHCb [2]. The inner structure however still remains unclear.

This work is based on observations that were made in the strange quark sector. In 2012, CBELSA/TAPS discovered an unexpected cusp in the $\gamma p \rightarrow K^0 \Sigma^+$ cross section, which could be explained by the same model that was used to predict the P_C pentaquark states at LHCb [6] (Fig. 2.1). It predicts a $K^* \Sigma$ resonance that interferes destructively with intermediate $K^* \Lambda$ and $K^* \Sigma^+$ states that feed the $\gamma p \rightarrow K^0 \Sigma^+$ cross section below the $K^* Y$ threshold. Above the $K^* Y$ threshold these processes no longer contribute and the cross section drops rapidly [7].

The same model also predicts a constructive interference of the resonance with the intermediate states in the reaction $\gamma n \rightarrow K^0 \Sigma^0$. The observance of this peak is the topic of K. Kohl's doctoral thesis [3] and would strongly hint at the existence of hadronic molecules in the strange quark sector. Though her results are consistent with the existence of a peak at 1750 MeV (the K^* threshold region) in the reaction $\gamma n \rightarrow K^0 \Sigma^0$, the observed enhancement could also be a result of statistical fluctuations (Fig. 2.2) [3, sec. 7.4]. The data at threshold was also compared to existing experimental data from A2 Collaboration and theoretical predictions from T. Mart, that both agree with the observed elevation in

position and width.

Furthermore, the perceived structure could only be seen in the most forward accessible angular range of $(0.2 < \cos\theta_{cm}^K < 0.5)$ (cm = center of mass). The theoretical calculations are so far limited to a total cross section, while an angular dependent prediction is not yet available. Since the cusp in the $\gamma p \to K^0\Sigma^+$ was most distinct in extreme forward direction $(0.7 < \cos\theta_{cm}^K < 1.0)$, it is however feasible for the incidental peak in the $\gamma n \to K^0\Sigma^0$ decay to appear correspondingly.
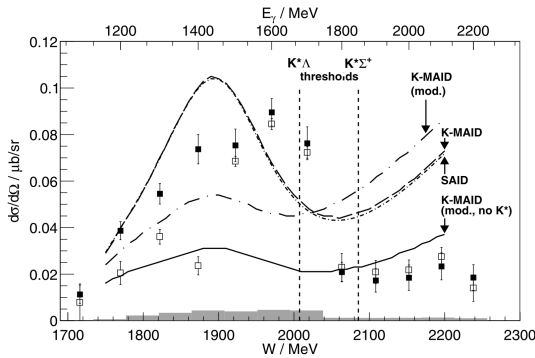
Fig. 2.1: Differential cross section for the reaction $\gamma p \to K^0\Sigma^+$, observed by the CBELSA/TAPS Collaboration for an angular range of $(0.7 < \cos\theta_{cm}^K < 1.0)$. Clearly visible is a strong cusp right at the $K^*\Lambda$ and $K^*\Sigma$ thresholds (marked by the dotted line). Figure taken from [6, p.184].
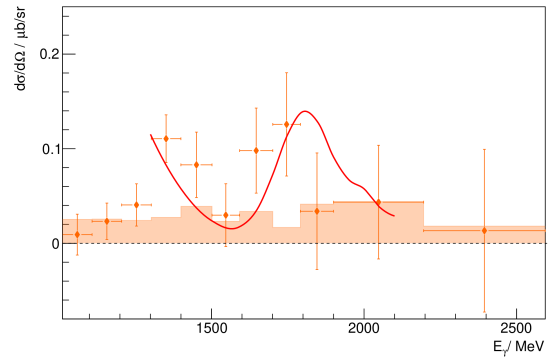
Fig. 2.2: Error weighted average of the differential cross section for the reaction $\gamma n \to K^0\Sigma^0$, observed in K. Kohl's doctoral thesis for an angular range of $(0.2 < \cos\theta_{cm}^K < 0.5)$. Overlayed is the theoretical prediction for the total cross section from Ramos et al. [7] at an arbitrary scale. Figure taken from [3, p.72].

To confirm the observed peak in the $\gamma n \to K^0\Sigma^0$ cross section, the statistical precision needs to be increased. Additionally it would be beneficial to extend the angular range further to the forward region.

Both requirements can be achieved by including the charged decay of the $K^0_S \to \pi^-\pi^+$, due to the possibility of measuring the charged particles in the forward spectrometer.

The main focus of this thesis is to investigate the feasibility to reconstruct this decay.

3 BGOOD Experimental Setup

The information in this section is taken from the technical paper of BGOOD [8], unless stated otherwise.

3.1 Particle accelerator ELSA

The BGOOD experiment receives high energy electrons from the **El**ectron **S**tretcher **A**ccelerator (ELSA), stationed in Bonn. [9]
The accelerator consists of three components (Fig. 3.1). In the first stage the electrons are emitted from a thermal gun and launched into the linear accelerator LINAC, where they are accelerated to an energy up to $26\,\text{MeV}$. These electrons are then introduced into the booster synchrotron, where they are accelerated to beam energies from $0.5\,\text{GeV}$ up to $1.6\,\text{GeV}$. Finally, the electrons are fed into the stretcher ring. This procedure repeats multiple times in a row with intervals of $2\,\text{ns}$, until the ring is completely filled with electrons. These are then accelerated to an energy up to $3.2\,\text{GeV}$, before being extracted to an experiment. This approach provides an almost continuous current of electrons, which is beneficial for the experiments ($\rightarrow$ Crystal Barrel and BGOOD).
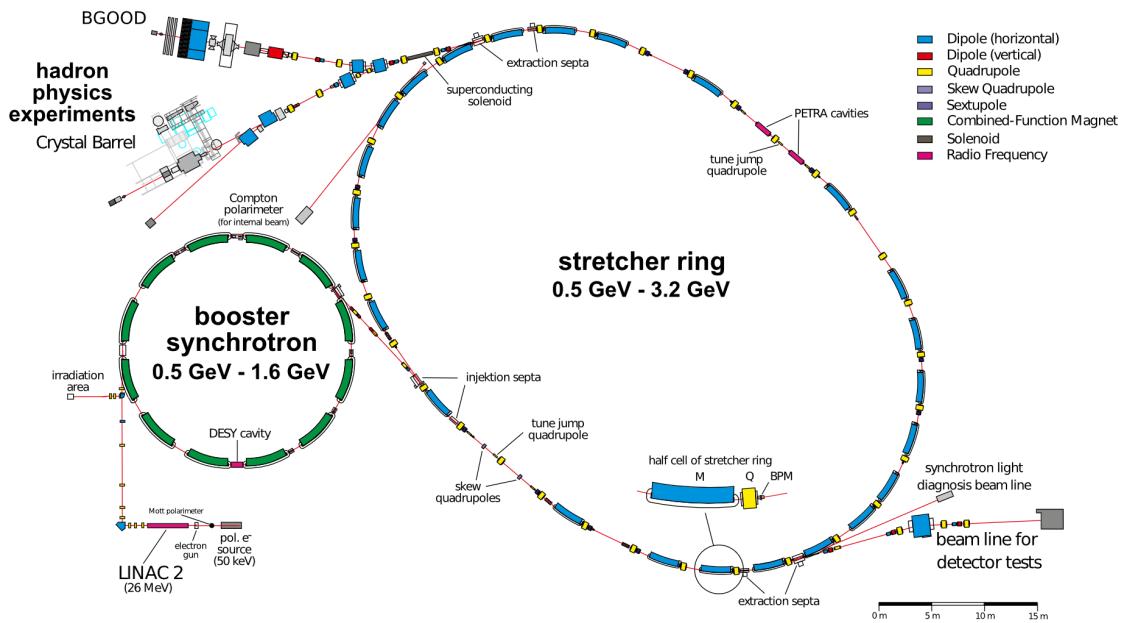

Fig. 3.1: Setup of ELSA. Figure taken from [8, p. 3].

3.2 BGOOD

An overview of the experimental setup of BGOOD, showing the main detector components, is depicted in Figure 3.2. The incoming electron beam is converted to a photon beam by the tagging system before transferring to the target. To provide the neutron for the reaction $\gamma n \to K^0 \Sigma^0$, the target consists of liquid deuterium; a liquid hydrogen target to provide a reaction with a proton would also be possible. Surrounding the targeting area is the central detector, followed by intermediate detectors and the forwards spectrometer.
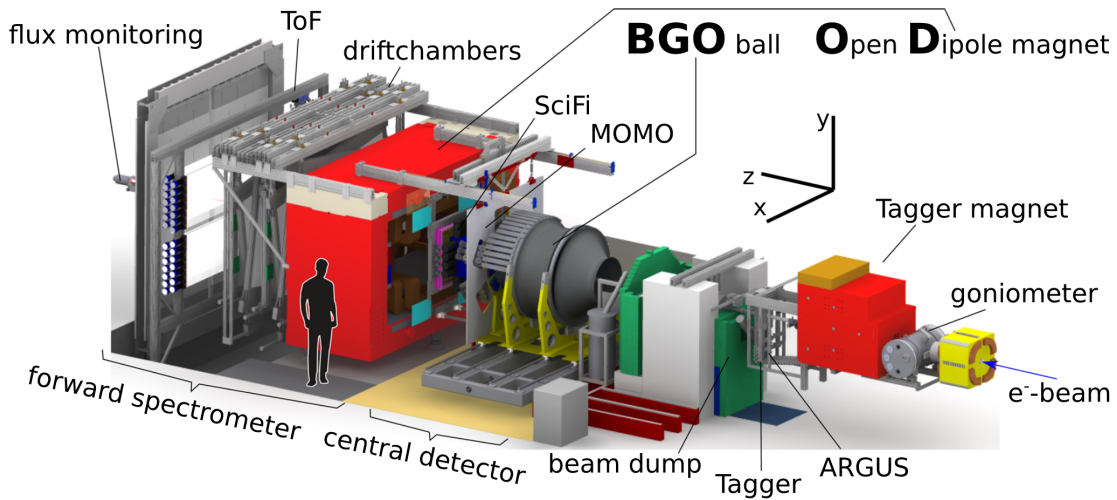
Fig. 3.2: Schematic representation of the BGOOD experiment with the main detector components. Figure taken from [8, p. 5].

3.3 Photon tagging system

As a big part of the BGOOD-experiment consists of studying photoproductions, the provided electron beam is converted to a photon beam via bremsstrahlung.
This is done by aligning a radiator (primarily out of copper or diamond) with the path of the electron beam. The created photons are then transferred to the tagging system, which determines their energy. Notably, the atom structure of the radiator influences the polarisation of the photons; as the polarisation has no impact on the contents of this work, it will therefore not be further regarded.

Given that the nature of bremsstrahlung results in a continuous spectrum, the energy of the resulting photons needs to be determined, in order to be able to recreate the reaction. This is done by separating the bremsstrahlung photon and electron using a magnet; while the photons can pass the magnetic field unaffected and are transferred into the experiment, the electrons are bent due to the Lorentz force. Given that the radii

of the deflections depend on the momenta of the electrons, it is possible to deduce their post-bremsstrahlung energy E' from their impact points on a scintillator hodoscope. The energy E_γ of the photon can now be calculated by subtracting the electron energy E' post-bremsstrahlung from the original electron beam energy E_0.
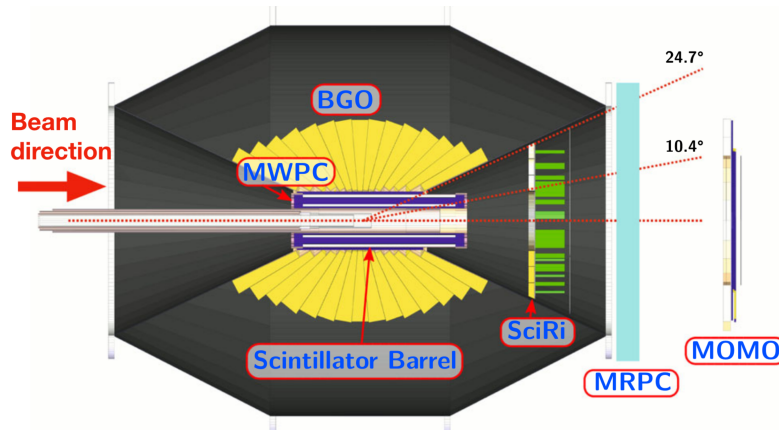
The schematic setup of this process can be seen in Figure 3.3.
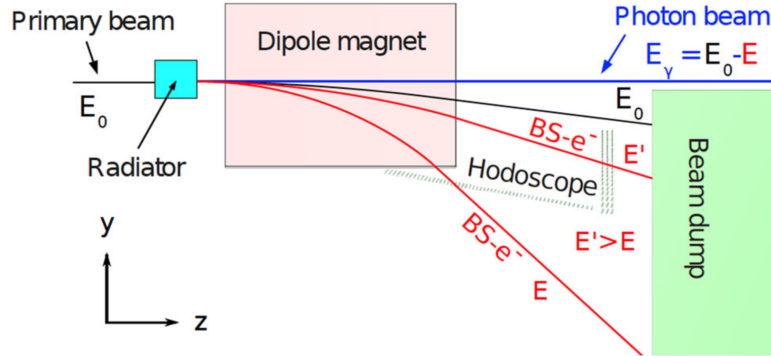
Fig. 3.3: Setup of the beam photon γ_T tagging system. Figure taken from [8, p. 12].

3.4 Detectors

There are two main detectors surrounding the target: the BGO crystal calorimeter (or BGO-ball) and the forwards spectrometer (Fig. 3.4).

Fig. 3.4: Setup of the detectors. Figure taken from [8, p. 6].

3.4.1 Central Detectors

The BGO-ball encloses the target cell in full azimutal range ϕ and in a polar angle range θ from 25° to 155°. It is made up of 480 bismuth germanate crystals $\mathbf{Bi}_4(\mathbf{GeO}_4)_3$, which give

the experiment the first half of its name. The crystals are connected to photomultipliers to register the scintillation light yield. This setup results in a temporal resolution of 2 ns and is optimised to measure the energy deposition of photons. It is also possible to detect charged particles, though a full energy deposition in the detector is unlikely and therefore a source of uncertainty whilst recreating a particle.

Whether a detected particle is charged or not is determined by the scintillator barrel, consisting of 32 plastic scintillator bars. Since the detection efficiency for charged particles is 98 %, whereas the efficiency for neutral particles is just 1 %, this setup is reliable to distinguish between them ([8, p. 7]).

Additionally, the **M**ulti-**W**ire **P**roportional **C**hambers (MWPC) is designed to help reconstructing particle tracks. However the software to analyse the recorded data is the subject of continuing development and was not available for this work.

3.4.2 Forward Spectrometer

The more forward polar angular range from 1.5° to 12° is covered by the forward spectrometer. The core of the spectrometer is a large **O**pen **D**ipole magnet, which gives the experiment the second half of its name (BG**OD**) and produces magnetic fields up to 0.4 T. The kinetic energy of a passing particle is measured by tracking its path with scintillating fibre detectors (MOMO and SciFi2) in front of the magnet and eight drift chambers behind it. Due to the curved trajectory of charged particles in the magnetic field (Lorentz force) the momentum can be determined. In addition with time-of-flight (ToF) measurements behind the drift chambers, the mass of the detected particles can be determined.

3.4.3 Intermediate Detectors

Between the BGO-ball and the forwards spectrometer (in a angular range of 10° to 25°) a **Sci**ntillating **Ri**ng detector (SciRi) provides information about the position of charged particles. An alternative **M**ulti-**R**esistive **P**late **C**hamber (MRPC) with a greater acceptance gap and thus better time and momentum resolution is planned for future use.

4 Analysis Tools

The analysis for this work is based on ExPlORA (**Ex**tended **Pl**uggable **O**bjectoriented **R**OOTified **A**nalysis), an extension to the ROOT framework, based on C++. The ExPlORA framework provides ample preanalysis steps like decoding, hit and track reconstruction and calibration (for a detailed description see [10]).

The ExPlORA framework is able to simulate the initial and final states of the examined reaction (here: $\gamma n \rightarrow \Sigma^0 K^0$), based on Monte Carlo simulations, using Geant4 [11]. Notably, the generated data can be processed using the same steps as real data.

As this work is concentrating on a neutron target, the consideration of Fermi motion is necessary. In contrast to the single proton nucleus of a hydrogen target, the neutron of the deuteron is part of a bound system. Though the binding energy of 2.225 MeV is relatively small compared to the neutron and proton mass (939.565 MeV and 938.272 MeV [4, p. 6]), there is a momentum distribution of the nuclei that influences the momenta of the decay particles ($\rightarrow$ Fermi motion) and amounts to around 80 MeV on average. A detailed explanation of the event generation and the implementation of the Fermi motion in the particle simulation can be found in the doctoral thesis of K. Kohl [3, p. 25].

5 $\gamma n \to K_S^0 \Sigma^0$ event selection

This chapter aims to describe the methods used to reconstruct the reaction $\gamma n \to K_S^0 \Sigma^0$.

As mentioned in the introduction, this work will examine if the reconstruction of the kaon decay into two charged pions is possible and could increase the statistics for further analyses. The full decay path is

$$\gamma_{\mathrm{T}} n \;\to\; K^0 \Sigma^0 \;\to\; \gamma p \pi^- \pi^- \pi^+,$$

wherein γ_{T} denotes the beam photon and γ the photon from the Σ^0 decay. The following decays are regarded [4]:

$$\Sigma^0 \xrightarrow{100\,\%} \gamma \Lambda^0$$
$$\Lambda^0 \xrightarrow{63.9\,\%} p\pi^-$$
$$K^0 \xrightarrow{69.2\,\%} \pi^+\pi^-.$$

In this analysis, the positively charged proton was measured in the forwards spectrometer, while the other charged particles (the three pions) were detected in the BGO-ball and SciRi. The neutral photon was detected in the BGO-ball.

In the following passages several selection cuts are applied to reduce combinatorics. The π fitting best to a Λ is identified (5.2) and the photon is checked to be from the Σ^0 decay (5.3). Since a free neutron target does not exist, the examined data was taken with a deuterium target. Thus, it is expected that a big part actually reacted with the proton, instead of the targeted neutron. The removal process is described in section 5.4.

As the examined $\gamma n \to K_S^0 \Sigma^0$ reaction only exists for beam energies above approximately $1000\,\mathrm{MeV}$, all events happening with beam energies $E_{\gamma_{\mathrm{T}}}$ below that threshold were excluded.

5.1 Pion momentum reconstruction

As mentioned in the experimental setup, a charged particle in the central calorimeter will potentially not deposit all of its energy in the crystals. In contrast to the electromagnetic showers a photon induces in the BGO crystals by pair-production and bremsstrahlung, heavy charged particles loose their energy through Bethe-Bloch ionization, which results in a much straighter pathway (Fig. 5.1).

Therefore the direction of the passing charged particle is known, while its momentum is not. Nonetheless it is possible to calculate the momentum of the three incompletely measured pions in the BGO and SciRi by momentum conservation, because the other four involved decay particles are known within uncertainties and Fermi motion:

$$p_z(\gamma_{\mathrm{T}}) + p_z(n) \;=\; p_z(p) + p_z(\gamma) + K_1 \cdot \hat{p}_z(\pi_1^-) + K_2 \cdot \hat{p}_z(\pi_2^-) + K_3 \cdot \hat{p}_z(\pi_3^-). \qquad (5.1)$$
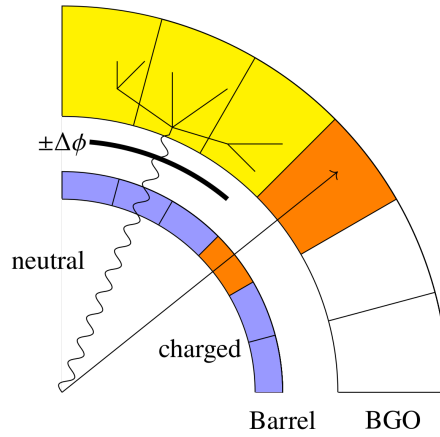
Fig. 5.1: Rough representation of the energy deposition of a neutral (left) and a charged (right) particle in the BGO crystals. Figure taken from [3, p. 30].

By equating p_x and p_y similarly to the z component of the momentum, this results in a set of three equations with three unknowns (K_1, K_2 and K_3), which is solvable. [12]

5.1.1 Consistency check of the momentum reconstruction

To check the consistency and the limits of the momentum reconstruction, Monte Carlo simulated data of $\gamma n \rightarrow K^0 \Sigma^0$ is used, as therein the „true " momentum is known and can be compared to the reconstructed momentum.

When using the true generated particle directions while also including the target nucleons momentum (Fermi motion), the smearing due to the momentum reconstruction calculation is minimal (Fig. 5.2). As expected, this can be seen as a discrete delta distribution around zero (Fig. 5.2, red distribution) . When using (real) measured data it is not possible to include the Fermi motion, instead the target nucleon is assumed to be at rest. Thus the momentum resolution is significantly broadened to $\sim100\,\mathrm{MeV\,c^{-1}}$ (Fig. 5.2, green distribution). Additionally considering detector resolution (thus regarding „measured" data) results in a further broadening of the momentum resolution to roughly $200\,\mathrm{MeV\,c^{-1}}$ (Fig. 5.2, blue distribution). Given the restrictions, the determination of the pion momenta from momentum conservation is possible. However, in a realistic scenario the momentum resolution is considerable and of the order of $\sim200\,\mathrm{MeV\,c^{-1}}$.
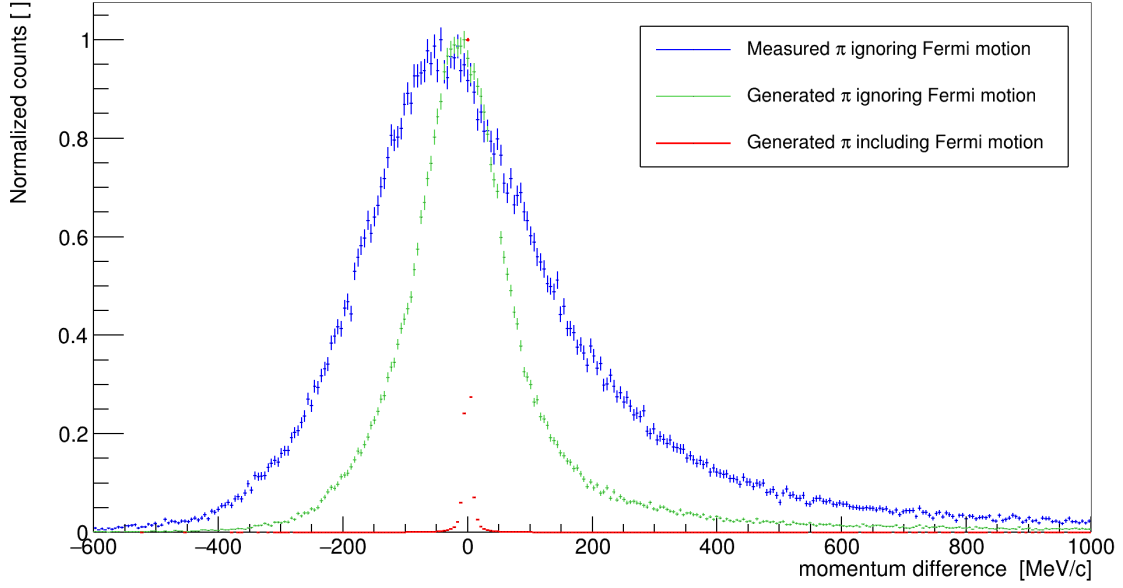
Fig. 5.2: Distributions regarding the difference between true and calculated π momenta for generated pions with Fermi motion included (green) and without (red) Fermi motion (thus assuming the target at rest) and for measured pions with Fermi motion (blue).

5.2 Λ^0 reconstruction – Angle between Λ^0 and its decay particles p and π^-

After the decay of the Λ^0 into a p and a π^- the direction of the Λ^0 and the p are approximately the same in the laboratory frame, due to them having nearly the same mass (cf. Fig. 5.3 and 5.4). This constraint provides a first indication as to which of the three measured charged particles in the central detector attributes best (or at all) to the reconstruction of the Λ^0.

The angle α_{max} is at a maximum of 180° when the Λ is at rest (Fig. 5.4). The more the kinetic energy of the Λ increases, the more the decay particles are boosted in the direction of the decaying Λ. Because the p is a lot heavier than the π^- it is affected stronger and its maximum angle $\alpha_{\text{max},p}$ drops very quickly, while the π^- angle can reach 180° up to a kinetic energy of about 300 MeV.

To account for detector resolution, an additional 10° is allowed atop of the maximum angle given. When plotting $p\pi$ invariant mass, a peak at the Λ^0 mass can be observed, including a large tail to larger masses (Fig. 5.5; cf. Supplementary Fig. A.1). After selecting only events that fulfill the above mentioned angle condition, this tail is drastically reduced. The applied angle condition cuts away a majority of falsely reconstructed Lambdas, as the peaks are becoming more discrete with the cut applied and remain near the expected Lambda mass of $1115.7 \, \text{MeV} \, \text{c}^{-2}$ ([4, p. 172]). When regarding only the best recreated
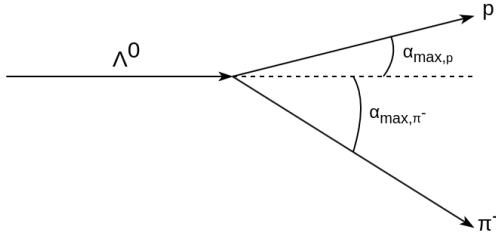
Fig. 5.3: Depiction of the $\Lambda^0 \rightarrow p\pi^-$ decay. The angles α_{max} represent the maximum possible angle between the decaying Λ^0 trajectory and the respective decay particles in the lab frame. Figure adapted from [3, p. 35]
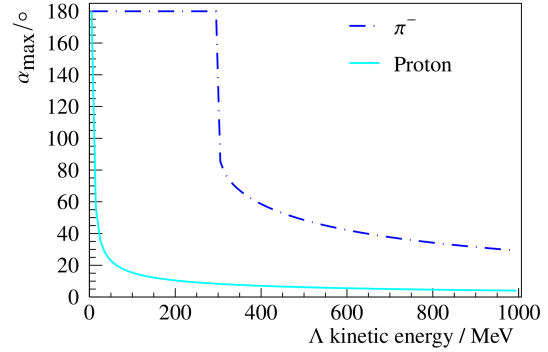
Fig. 5.4: Graphs of the maximum possible angles α_{max} in the lab frame between the decaying Λ^0 and the generated p and π^- as function of the Λ kinetic energy. Figure taken from [3, p. 36]
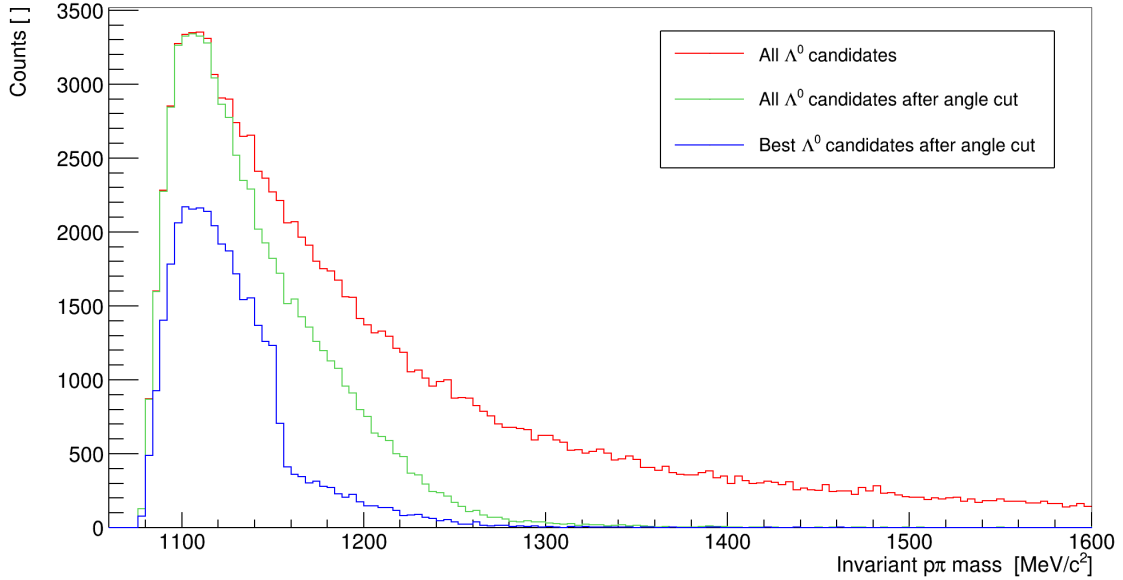
Fig. 5.5: Reconstructed simulated Λ^0 candidate from p and any π. The red distribution depicts all reconstructed Λ^0, while the green curve only contains Λ^0 candidates that comply with the above described angle condition. The blue distribution shows only those reconstructed Λ^0 that fulfill the condition **and** coincide best with the expected Λ^0 mass.

Λ^0 according to its mass, this effect intensifies. Proceeding, only events with the best recreated Λ^0 will be regarded further.

5.3 Σ^0 reconstruction - Photon γ energy cut

After selecting the most fitting π for the Λ^0 reconstruction by applying the angle condition (cf. section 5.2), the Σ^0 can be reconstructed by adding the measured photon γ.

The photon energy for the examined prominent decay $\Sigma^0 \rightarrow \gamma\Lambda^0$ is discrete in the Σ^0 resting frame and can be calculated:

$$m_{\Sigma^0,0}^2 = E_{\Sigma^0}^2 - ||\vec{p}_{\Sigma^0}|| = (E_{\Lambda^0} + E_\gamma)^2 - \left(|\vec{p}_{\Lambda^0}| - |\vec{p}_\gamma|\right)^2 \tag{5.2}$$

$$= (E_{\Lambda^0} + E_\gamma)^2 = \underbrace{m_{\Lambda^0}^2 + E_\gamma^2}_{E_{\Lambda^0}} + 2E_{\Lambda^0}E_\gamma + E_\gamma^2 \tag{5.3}$$

$$= m_{\Lambda^0}^2 + 2m_{\Sigma^0}E_\gamma \tag{5.4}$$

A transposition of equation 5.4 results in the expected photon energy (masses from [4]):

$$E_\gamma = \frac{m_{\Sigma^0}^2 - m_{\Lambda^0}^2}{2m_{\Sigma^0}} \approx \frac{1192.6\,\mathrm{MeV}^2\,\mathrm{c}^{-2} - 1115.7\,\mathrm{MeV}^2\,\mathrm{c}^{-2}}{2 \cdot 1192.6\,\mathrm{MeV}\,\mathrm{c}^{-2}} \approx 74.4\,\mathrm{MeV} \tag{5.5}$$

To sort out as many events as possible that do not conform to the regarded Σ^0 decay, only photon energies within around one sigma σ of the expected energy of $74.4\,\mathrm{MeV}$ are taken into account. These boundaries are set to be $63\,\mathrm{MeV}$ for the lower cut and $86\,\mathrm{MeV}$ for the higher bound (Fig. 5.6).
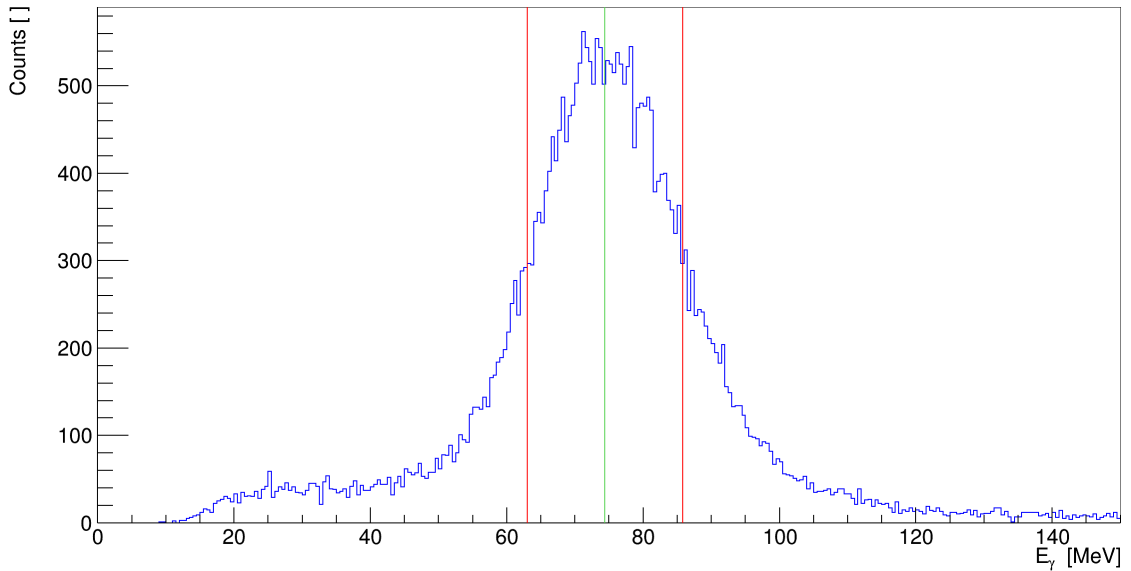
Fig. 5.6: Simulated photon energy distribution. For the regarded Σ^0 decay the photon should have a discrete energy of around $74.4\,\mathrm{MeV}$ (green line). To exclude the majority of other photon sources, only the events with photon energies within around one σ of $74.4\,\mathrm{MeV}$ are considered (red lines).

Regarding the simulated invariant Σ^0 candidate mass distribution, the cut increases the distinctness of the peak (Fig. 5.7; cf. Supplementary Fig. A.2).
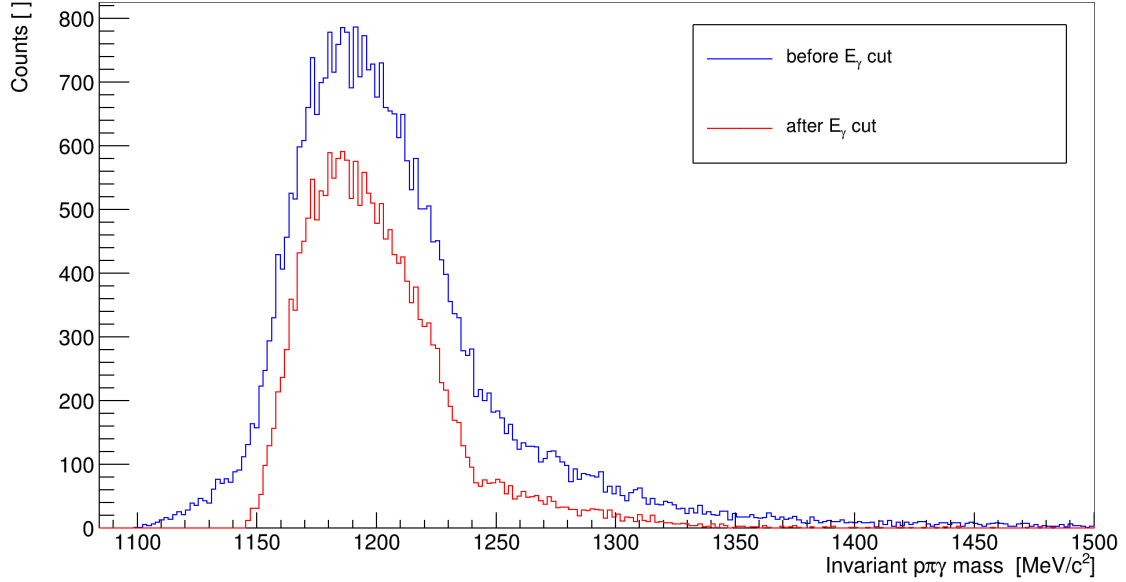

Fig. 5.7: Reconstructed simulated $p\pi\gamma$ invariant mass distribution with (red) and without (blue) photon energy cut.

The remaining two pions from the best recreated Σ^0 candidate are used to recreate the invariant $K_S^0 = \pi^+\pi^-$ mass (Fig. 5.8).

There is no visible peak at the K^0 mass of $497.61\,\mathrm{MeV\,c^{-2}}$ [4, p. 42] in measured data (blue distribution). Despite all preceding selection cuts the $\pi\pi$ invariant mass distribution is too broad to be distinguishable from the background. This is likely due to the momentum resolution (sec. 5.1). In contrast, the subtraction of the Fermi motion in simulated data results in a very discrete peak around the expected K^0 mass (red distribution). That the Fermi motion has a big impact on the analysis can be seen by the much broader distribution of the generated invariant $\pi\pi$ mass with Fermi motion (green distribution).

Considering the lack of viable selection cuts for the $K^0 \to \pi^+\pi^-$ decay, it is more promising to infer the kaon as missing mass to the reconstructed best Σ^0 candidate:

$$m_{\mathrm{miss},\Sigma^0}^2 = \left(P_{\gamma_{\mathrm{T}}} + P_n - P_{\Sigma^0}\right)^2. \tag{5.6}$$
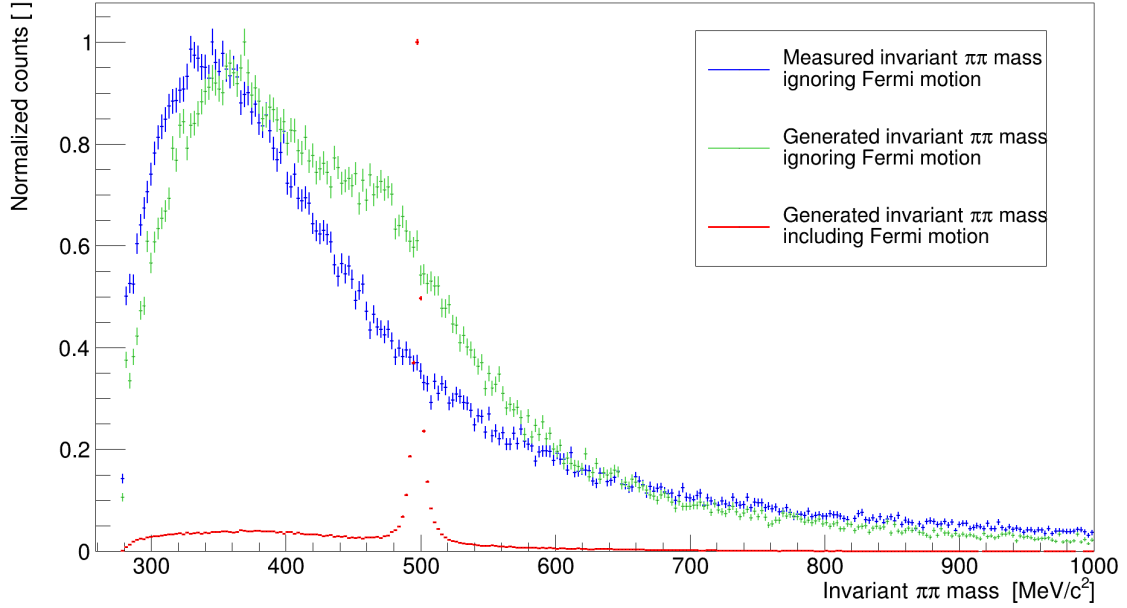
Fig. 5.8: Recreated $\pi\pi$ invariant mass as sum of two generated pions ignoring (green) and including (red) Fermi motion and of two measured pions ignoring Fermi motion (blue).

5.4 Subtracting the proton target background

After executing the above mentioned Σ^0 photon energy cut (sec. 5.3), as well as applying the Λ^0 decay particles angle condition (sec. 5.2), there still remains a lot of background in the real data reconstructions. As mentioned before, the major contribution to this background is expected to come from falsely assuming a reaction with the neutron, when in fact it comes from the in deuterium contained proton instead.

To remove this background, the same analysis is repeated with a hydrogen data set, scaled by luminosity and subtracted:

$$\text{yield}_D = \text{yield}_n + \text{yield}_p \quad \Leftrightarrow \quad \text{yield}_n = \text{yield}_D - \text{yield}_p. \tag{5.7}$$

The differential cross section $\mathrm{d}\sigma/\mathrm{d}\Omega$ of a reaction can be obtained by the following calculation:

$$\frac{\mathrm{d}\sigma}{\mathrm{d}\Omega} = \frac{Y}{F \cdot \delta \cdot \epsilon \cdot \mathrm{d}\Omega} = \frac{Y}{\mathcal{L} \cdot \epsilon \cdot \mathrm{d}\Omega}, \tag{5.8}$$

wherein Y is the yield, F the photon flux, δ the area density of the target, ϵ the reconstruction efficiency, $\mathrm{d}\Omega$ the regarded angular range and $\mathcal{L}$ the luminosity. It can be used to obtain the scaling variables when comparing two data sets (here: deuterium

data and hydrogen data):

$$\frac{\frac{d\sigma}{d\Omega}_D}{\frac{d\sigma}{d\Omega}_H} = 1 = \frac{Y_D \cdot \mathcal{L}_H \cdot \epsilon \cdot d\Omega}{Y_H \cdot \mathcal{L}_D \cdot \epsilon \cdot d\Omega} \qquad (5.9)$$

$$\Leftrightarrow \quad Y_D = \frac{\mathcal{L}_D}{\mathcal{L}_H} \cdot Y_H = \frac{F_D \cdot \delta_D}{F_H \cdot \delta^H} \cdot Y_H. \qquad (5.10)$$

Additionally the hydrogen data has to be smeared to take the Fermi motion of the quasi free nucleon in the deuterium into account. The required simulations and calculations were beyond the scope of this thesis. However, as shown in [3, p. 37-39], the effect is not very strong, resulting in a good approximation even when excluding Fermi smearing.

The area density δ of the used target is calculated with $\delta = d \cdot l$, wherein d is the target density and l the target length (here in both cases 11.1 cm). The densities d of the deuteron and hydrogen targets were taken from [13, p. 36]:

$$d_D = 5.053 \times 10^{-8}\,\mu\text{b}^{-1}\,\text{cm}^{-1} \quad \text{and} \quad d_H = 4.237 \times 10^{-8}\,\mu\text{b}^{-1}\,\text{cm}^{-1}. \qquad (5.11)$$

The photon flux for the hydrogen and deuterium data can be seen in Figure B.1.
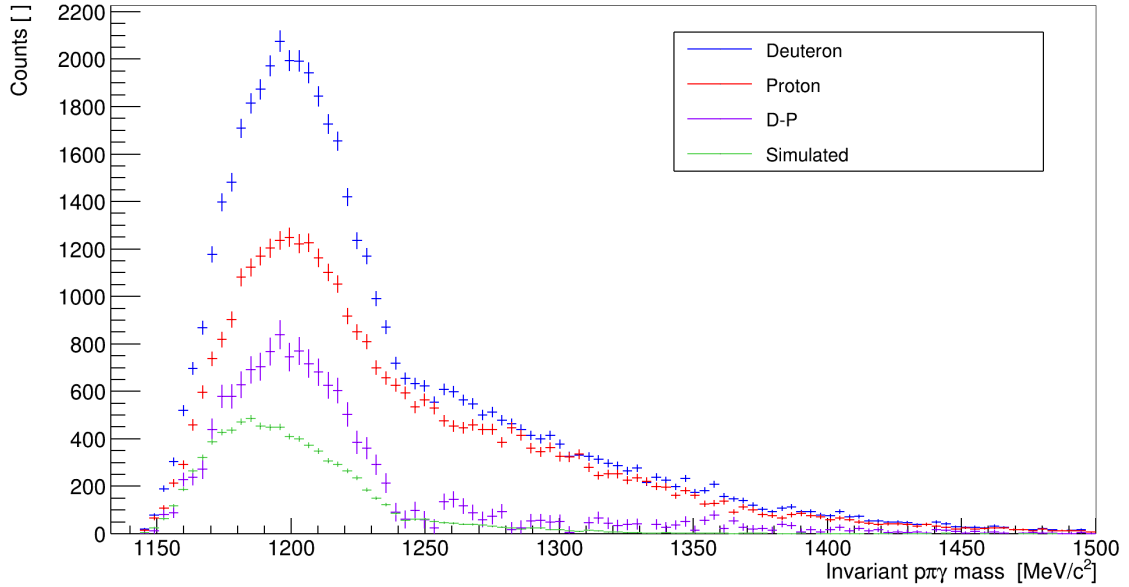
Fig. 5.9: $p\pi\gamma$ invariant mass. The blue distribution shows deuterium data, red is hydrogen data, violet the subtraction (deuteron - proton data) and green is simulation.

The reconstructed $p\pi\gamma$ invariant mass after all preceding selection cuts for deuteron (blue), hydrogen (red), deuteron - proton (violet) and arbitrarily scaled simulated (green) data shows a Σ^0 peak in the hydrogen data, presumably due to the reaction $\gamma p \rightarrow K^+ \Sigma^0$

(Fig. 5.9). When subtracting the hydrogen data from the deuterium data most of the background disappears and there is a prominent peak left around the expected Σ^0 mass of 1192.64 MeV, which is consistent with the peak seen in the simulated data (Fig. 5.9, green distribution).

The reconstructed missing mass to $p\pi^-\gamma$ for deuteron (blue), hydrogen (red), deuteron - proton (violet) and simulated and arbitrarily scaled (green) data show an elevation at the expected K^0 mass (Fig. 5.10). Notably, the data contained entries with negative masses. Since these are physically unfeasible they were excluded from the analysis.
Although there is an elevation at the expected K^0 mass, a clear distinction from background is difficult.
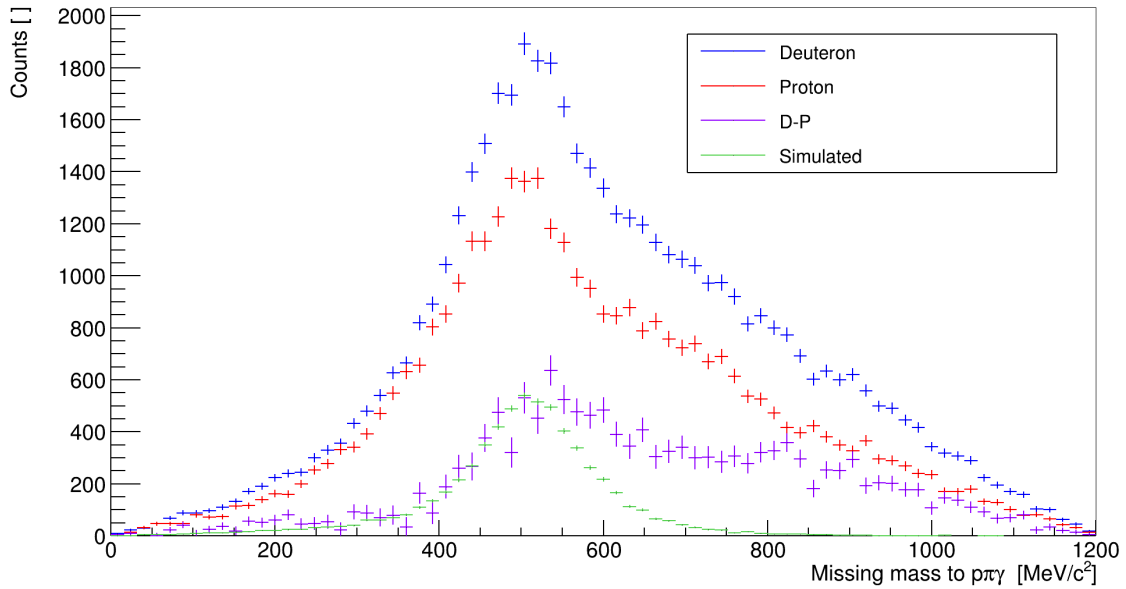
Fig. 5.10: Missing mass to $p\pi\gamma$. The blue distribution shows the missing mass in deuteron data, red in hydrogen data, violet with the subtraction (deuteron - proton data) and green in arbitrarily scaled Monte Carlo simulation of $\gamma n \to K^0\Sigma^0$.

6 $\gamma n \to K_S^0 \Sigma^0$ reconstruction efficiency

The reconstruction efficiency describes the probability to detect and reconstruct an event as a function of beam energy E_γ and $\cos\theta_{cm}^K$. It is determined from simulated Monte Carlo data as the ratio of reconstructed events, divided by all generated events and includes all detector efficiencies and branching ratios:

$$\mathrm{RE}(E_\gamma, \cos\theta_{CM}^K) = \frac{N_{\mathrm{reconstructed}}(E_\gamma, \cos\theta_{CM}^K)}{N_{\mathrm{generated}}(E_\gamma, \cos\theta_{CM}^K)}. \tag{6.1}$$

There are several limiting factors to the efficiency in addition to the branching ratios mentioned in the particle selection (sec. 5); firstly it is reduced by 50% due to the ability of the detectors to only detect the eigenstate K_S^0. Additionally the probability of a proton going in the forwards spectrometer is just of the order of 10%. Without including the detector resolution or other restrictions, this adds up to a maximum reconstruction efficiency of approximately 2%.
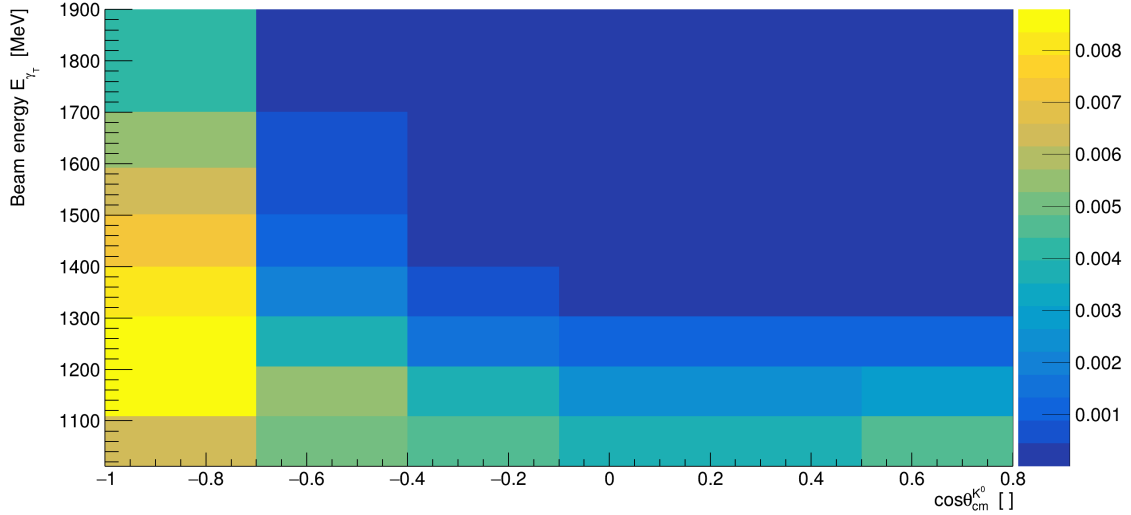
Fig. 6.1: Reconstruction efficiency RE for the reaction $\gamma n \to K^0 \Sigma^0$ from threshold to 1900 MeV in six bins of $\cos\theta_{cm}^{K^0}$.

The maximum reconstruction efficiency is around 0.9% in maximum backwards direction and just above threshold (Fig. 6.1). It is expected to detect most of the K^0 in the most backwards angular range, as the proton for the Σ^0 reconstruction is measured in the forwards spectrometer. The examination of the $K^0 \to \pi^+\pi^-$ decay in maximum forwards direction would require a π^+/π^- in the forwards spectrometer, or a p in the BGO. As the consequential analysis is a lot more complex it did not fit the scope of this work in respect to time.

With the present analysis it is not feasible to determine a cross section in forward angular range, due to the kinematic limit of the p being observed in the forward spectrometer. However, the covered region shows a reasonable value for the reconstruction efficiency, which is almost twice as high as in the previous work, where the RE was maximum $\sim 0.6\,\%$ [3]. The results of this thesis indicate that a reconstruction of a π in the forwards spectrometer or p in BGO would allow to determine a cross section also in forward direction using the presented tools.

7 Summary and outlook

This work aimed to provide an answer to the question whether the reaction $\gamma_T n \to K^0 \Sigma^0$ could be reconstructed via the charged $K^0 \to \pi^+\pi^-$ decay with the BGOOD experiment at the University Bonn. The complete final state consisted of $\pi^+\pi^- p\pi^-\gamma$.

Since the momenta of the three charged pions cannot be fully measured, they needed to be calculated from momentum conservation. In principle, the presented methods work, however, the momentum resolution is relatively broad ($\sim 200\,\mathrm{MeV\,c^{-1}}$) (see section 5.1). After executing several selection cuts including the decay photon of the $\Sigma^0 \to \Lambda\gamma$ decay and kinematic constraints on the Λ decay particles, it was possible to infer the K^0 as its missing mass.

To reduce background originating from the proton in the used deuterium target, a hydrogen data set was used. The same analysis was performed, with additional scaling by luminosity and subtracted from the deuterium data. In the resulting missing mass spectrum, an elevation around the K^0 mass is visible (Fig. 5.10). However, a clear distinction from the background remains difficult and additional studies are required.

For the reaction $\gamma_T n \to K^0 \Sigma^0$ the reconstruction efficiency shows a maximum of $0.9\,\%$ in the most backward accessible angular direction, which is larger than in the previous work. Due to the kinematic constraint of the p being observed in the forwards spectrometer, only backwards regions were accessible in this work. To access more forward regions it would be necessary to either identify the p in BGO, or a π in the forwards spectrometer. While more challenging, the shown analysis steps and tools would all be applicable.

This work showed that the reconstruction of $\gamma_T n \to K^0 \Sigma^0$ via the charged decay $K^0 \to \pi^+\pi^-$ is possible with reasonable efficiency and the cross section can most likely be determined over a large angular range.

# A $\gamma n \to K_S^0 \Sigma^0$ event selection cuts in real data
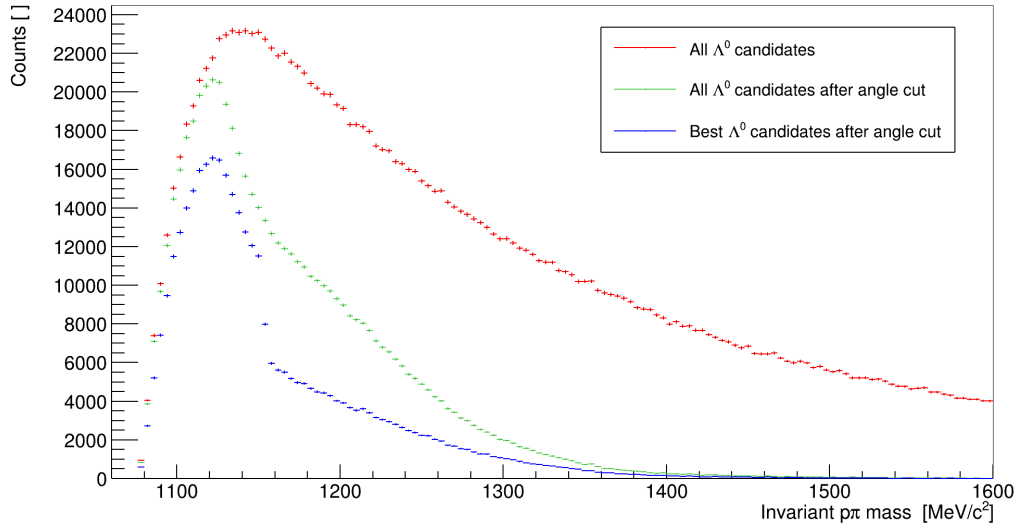
Fig. A.1: Reconstructed $p\pi$ invariant mass from real data. The red distribution depicts all recreated Λ^0 candidates, while the green curve only contains Λ^0 candidates that comply with the above described angle condition between the Λ and its decay particles. The blue distribution shows only those recreated Λ^0 candidates that fulfill the condition **and** coincide best with the expected Λ^0 mass.
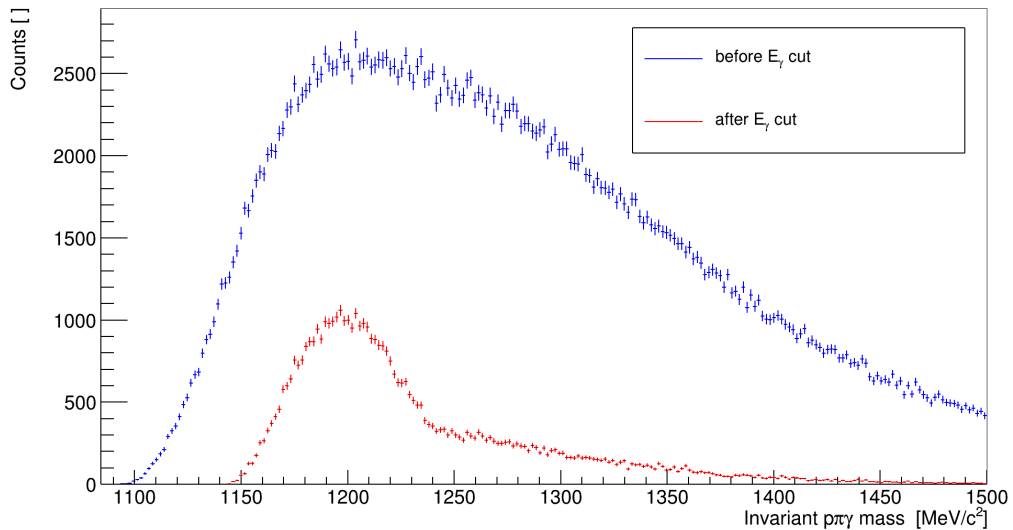
Fig. A.2: Reconstructed $p\pi\gamma$ invariant mass distribution with (red) and without (blue) γ energy cut in real data.

B Beam photon $\gamma_\mathbf{T}$ flux
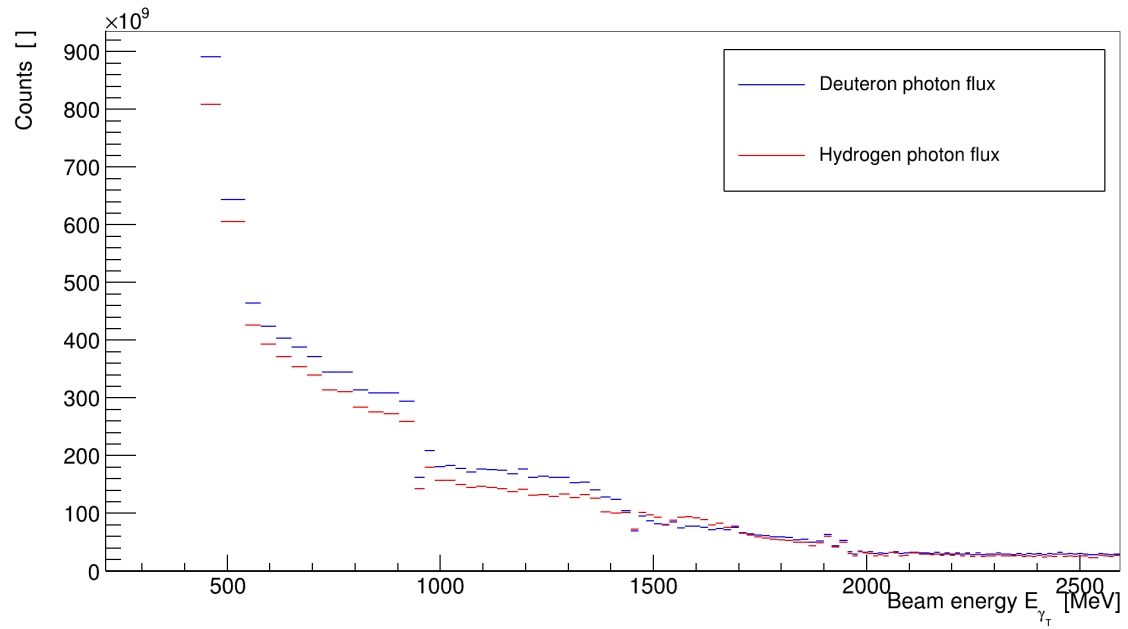
Fig. B.1: Beam photon γ_T flux for hydrogen (red) and deuteron (blue) data.

References

[1] S.-K. C. et al., 'Observation of a Narrow Charmoniumlike State in Exclusive $B^{\pm} \rightarrow K^{\pm}\pi^{+}\pi^{-}J/\psi$ Decays', Phys. Rev. Lett. **91**, https://doi.org/10.1103/PhysRevLett.91.262001 (2003).

[2] R. A. et al., 'Observation of a Narrow Pentaquark State, $P_C(4312)^+$, and of the Two-Peak Structure of the $P_C(4450)^+$', Phys. Rev. Lett. **122**, https://doi.org/10.1103/PhysRevLett.122.222001 (2019).

[3] K. Kohl, 'Measurement of the $\gamma n \rightarrow K^0\Sigma^0$ photoproduction at the BGOOD experiment and the relation to possible pentaquark states', https://hdl.handle.net/20.500.11811/9736 (2022).

[4] P. Z. et al., 'Particle Physics Booklet', (2022).

[5] F. G. et al., 'Hadronic molecules', Reviews of modern physics **90**, 10.1103/RevModPhys.90.015004 (2018).

[6] R. E. et al., 'Anomaly in the $K_S^0\Sigma^+$ photoproduction cross section off the proton at the K^* threshold', Physics Letters B **713**, 180–185 (2012).

[7] A. Ramos and E. Oset, 'The role of vector-baryon channels and resonances in the $\gamma p \rightarrow K^0\Sigma^+$ and $\gamma n \rightarrow K^0\Sigma^0$ reactions near the $K^*\Lambda$ threshold', Physics Letters B **727**, 287–292 (2013).

[8] S. A. et al., 'The BGOOD experimental setup at ELSA', Eur. Phys. J. A **56**, https://doi.org/10.1140/epja/s10050-020-00107-x (2020).

[9] W. Hillert, 'The Bonn Electron Stretcher Accelerator ELSA: Past and future', Eur. Phys. J. A **28**, 139–148 (2006).

[10] O. Freyermuth, 'Studies of ω Photoproduction off Proton at the BGO-OD Experiment, PhD thesis', https://hdl.handle.net/20.500.11811/7263 (2017).

[11] J. A. et al., 'Recent developments in Geant4', Nuclear Instruments and Methods in Physics Research Section A: Accelerators, Spectrometers, Detectors and Associated Equipment **835**, 186–225 (2016).

[12] K. Kohl, private communication.

[13] G. Scheluchin, '$\Lambda(1405)$ photoproduction with the BGO-OD experiment', https://hdl.handle.net/20.500.11811/8373 (2019).

List of Figures